



Impact of doped metals on urea-derived g-C₃N₄ for photocatalytic degradation of antibiotics: Structure, photoactivity and degradation mechanisms



Wei Yan^a, Li Yan^a, Chuanyong Jing^{a,b,*}

^a State Key Laboratory of Environmental Chemistry and Ecotoxicology, Research Center for Eco-Environmental Sciences, Chinese Academy of Sciences, Beijing 100085, China

^b University of Chinese Academy of Sciences, Beijing 100049, China

ARTICLE INFO

Keywords:

g-C₃N₄
Visible light photocatalysis
Metal doping
Photocatalytic degradation of antibiotics

ABSTRACT

Metal doping is an appealing modification strategy of graphitic carbon nitride (g-C₃N₄) to improve its photocatalytic activity. The interactions of g-C₃N₄ precursors with metals, however, has often been underappreciated, which can induce great impacts on g-C₃N₄ formation and properties. Herein, the impacts of metals (Na, K, Ca, Mg) on the morphology, structure, and photoactivity of urea-derived g-C₃N₄ were investigated. Our TEM and XPS results confirmed that the interactions of doped metals with urea precursors lead to the incorporation of O atoms from urea molecules into the framework of g-C₃N₄. Due to the synergistic effects of the metals and structural O atoms, doped g-C₃N₄ performed an elevated photodegradation of antibiotics under the visible light irradiation, which was attributed to the enhanced light-harvesting and reduced charge recombination. In addition, the doped metals presented uneven regulation on the band structures and morphology of g-C₃N₄. As a result, both superoxide and hydroxyl radicals were generated by g-CN-Na and g-CN-K, whereas, only superoxide radicals were involved in g-CN, g-CN-Ca and g-CN-Mg. Consequently, diversified photodegradation mechanisms for enrofloxacin (ENR) were observed that the g-CN, g-CN-Ca and g-CN-Mg reaction systems mainly attacked the piperazine moiety of ENR while g-CN-Na and g-CN-K provided additional photodegradation pathway by attacking quinolone core of ENR. The present work could provide new insights into further understanding of doping chemistry with g-C₃N₄.

1. Introduction

Graphitic carbon nitride (g-C₃N₄) is a promising photocatalysts for environmental remediation due to its suitable band gap (ca. 2.7 eV), low cost, and good chemical stability [1–3]. To extend the application of g-C₃N₄ under visible light irradiation, modifying its electronic bandgap structure by metal doping (Na, K, Fe, Co, Cu) [5–8] is a successful strategy [9]. Recently, both experimental [6,10,11] and theoretical [5] studies revealed that Na or K modulated the potentials of conduction band (CB) and valance band (VB) to extend the light absorption, leading to a significantly enhanced photodegradation performance of g-C₃N₄.

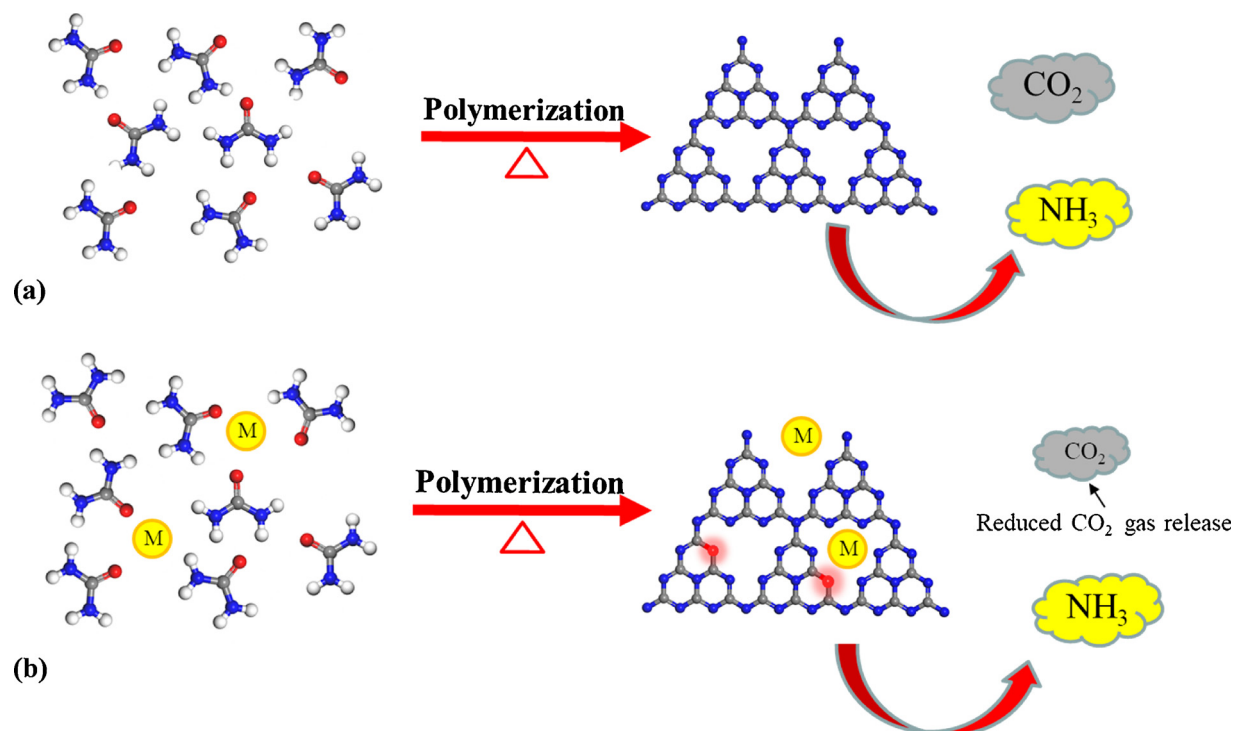
Nevertheless, it is arbitrary to fully attribute this enhanced activity to the sole change in the local electronic distribution of doped g-C₃N₄ [5]. Actually, given that the doped g-C₃N₄ is usually fabricated by the thermal condensation of the mixture of soluble cations with the

precursor of g-C₃N₄, the interactions between them may cause considerable impact on the formation of bulk g-C₃N₄, which has often been underappreciated. For example, urea has been demonstrated as an excellent precursor of g-C₃N₄ because the condensation of urea molecules can generate and release NH₃ and CO₂ gases (Scheme 1a), which make the produced g-C₃N₄ with high specific surface area and activities [4]. When urea is selected as the precursor of doped g-C₃N₄, due to the strong interaction between metals and the lone pair electrons of oxygen in urea, we hypothesized that metals may capture oxygen atom from urea into the framework of g-C₃N₄ (Scheme 1b). To our best knowledge, the molecular-level understanding of the impact of the heteroatom doping on the framework structure of urea-derived g-C₃N₄ and its consequent photophysical properties is still missing. Nevertheless, this knowledge is paramount important to fabricate doped g-C₃N₄ and realize its applications.

Herein, two alkali metals, K and Na, and two alkaline earth metals,

* Corresponding author at: State Key Laboratory of Environmental Chemistry and Ecotoxicology, Research Center for Eco-Environmental Sciences, Chinese Academy of Sciences, Beijing 100085, China.

E-mail address: cjing@rcees.ac.cn (C. Jing).



Scheme 1. Illustration of (a) urea condensation to synthesize g-C₃N₄ with the release of CO₂ and NH₃; (b) the reaction of urea and metals during condensation process causes the retention of O atoms into the g-C₃N₄ and less gas release.

Ca and Mg, were selected to investigate the interactions of different cations with urea and their impacts on the morphology and structure of urea-derived g-C₃N₄. The photodegradation performance and the involved mechanisms were evaluated by the photodegradation of three representative antibiotics (Fig. S1), namely, enrofloxacin (ENR), tetracycline (TCN), and sulfamethoxazole (SMX), considering their continuously increasing use and potential risks to the environment. The insights gained from the present work opened new door for further understanding of doping chemistry with g-C₃N₄.

2. Experimental section

2.1. Materials and synthesis

All chemicals were analytical reagent grade or higher and were used without further purification. Urea was applied as the precursor for the synthesis of porous doped g-C₃N₄. Typically, 12 g of urea was dispersed in 50 mL XBr or YBr₂ aqueous solution (3 wt %, X = Na, K, Y = Ca, Mg) and the mixture was vigorously stirred overnight at 80 °C. The prepared solid precursor was placed in a capped alumina crucible and then transferred into a muffle furnace. The crucible was annealed at 550 °C for 2 h with a ramping rate of 15 °C min⁻¹ and maintained for 2 h. The resultant yellow product (denoted as g-CN-Na, g-CN-K, g-CN-Ca, g-CN-Mg) was collected and ground in an agate mortar into powders (Fig. S2). For comparison, the undoped g-C₃N₄ (denoted as g-CN) was prepared in the same way without cation addition.

2.2. Characterization

The morphology and elemental mappings were characterized by a scanning transmission electron microscopy with high-angle annular dark-field (HAADF) detector (FEI Tecnai G2 F20 S-TWIN) operated at 200 KV. The crystal structures of the prepared samples were determined by powder X-ray diffraction (XRD) using an X'Pert PRO diffractometer (PANalytical, Netherlands) with Cu K α radiation. The Brunauer–Emmet–Teller (BET) specific surface area and

Barrett–Joyner–Halenda (BJH) pore size distribution were determined from N₂ adsorption–desorption isotherms measured at 77 K using an automated gas sorption instrument (ASAP 2020, U.S.A.). Total Organic Analyzer (Phoenix 8000) was used to perform TOC analysis. Elemental analysis was performed by an Elementar Vario EL III instrument (Elementar, Germany). X-ray photoelectron spectroscopy (XPS) and X-ray photoelectron valence-band (VB) spectra were recorded by using AXIS Supra by Kratos Analytical with an Al K α X-ray source (1486.8 eV). All XPS measurements were performed at a power of 150 W. The pass energies were set as 160 eV for survey, 40 eV for high-resolution, and 40 eV for VB spectra, respectively. The solid-state ¹³C cross-polarization magic angle spinning (CP-MAS) nuclear magnetic resonance (NMR) spectra were recorded by a Bruker Avance III 400 spectrometer at room temperature. The FTIR measurements were performed using a Thermo-Nicolet Nexus 6700 FTIR spectrometer using a standard KBr pellet technique. Each spectrum was recorded as the average of 128 scans with a resolution of 4 cm⁻¹ from 4000 to 600 cm⁻¹. The ζ potential was measured using a Zetasizer Nano ZS (Malvern Instrument Ltd., UK). UV-vis diffuse reflectance spectra (DRS) were obtained using a UV-vis spectrophotometer (UV-2450, Shimadzu, Japan) equipped with an integrating sphere assembly, while BaSO₄ was used as a reference. The photoluminescence (PL) emission spectra were measured on a fluorescence spectrometer (Varian, Cary Eclipse) at an excitation wavelength of 370 nm. Time-resolved fluorescence decay spectra were recorded by a FLS1000 Fluorescence Spectrometer (Edinburgh Instruments) with excitation at 375 nm. The photocurrent measurements and electrochemical impedance spectroscopy (EIS) were performed with a PGSTAT302N Electrochemical Workstation (Autolab, Switzerland) and the details are provided in the Supplementary information.

2.3. Photocatalytic activity measurements

Photocatalytic activity of the doped g-C₃N₄ was evaluated by the photodegradation of antibiotics (ENR, TCN, SMX). The details are provided in the Supplementary information.

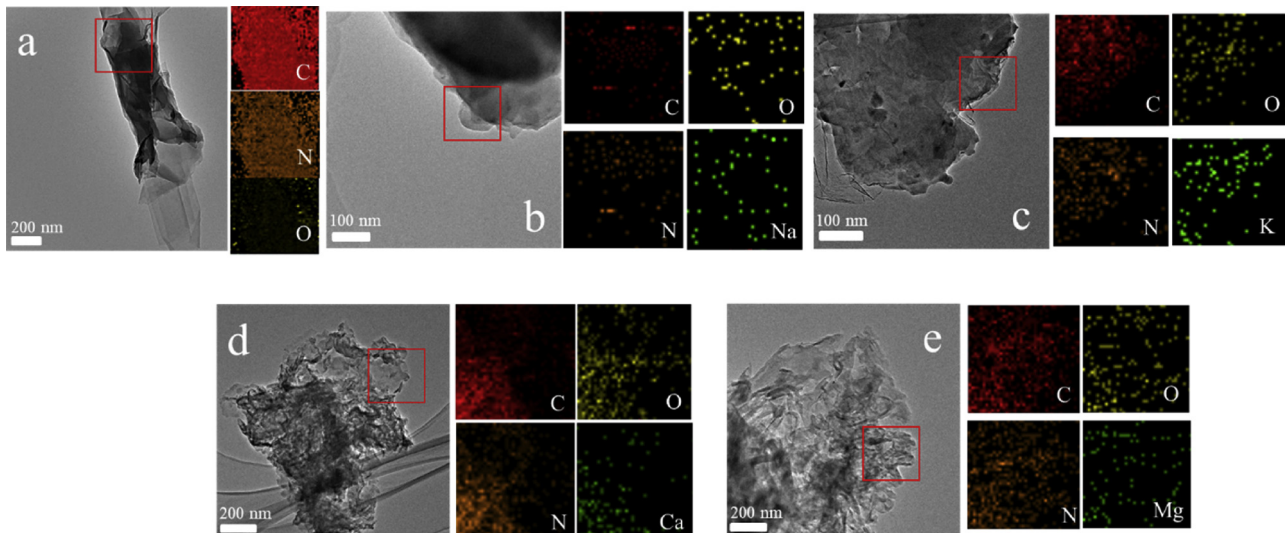


Fig. 1. HAADF-TEM images and elemental mapping of the selected red area for C, N, O, and doped metal atoms: (a) g-CN, (b) g-CN-Na, (c) g-CN-K, (d) g-CN-Ca, (e) g-CN-Mg. (For interpretation of the references to colour in this figure legend, the reader is referred to the web version of this article.)

2.4. Reactive oxygen species (ROS) analysis

The visible light induced ROS (i.e., superoxide anion radicals ($O_2^{\cdot -}$), hydroxyl radicals ($\cdot OH$)) with the catalyst was measured by the electron spin resonance (ESR) and the continuous flow chemiluminescence (CFCL) techniques. The radical scavenging experiments were also conducted to clarify the role of each ROS species in the photo-degradation process. The details are provided in the Supplementary information.

3. Results and discussion

3.1. Morphology and composition

The morphology of g-CN displayed a silk-like structure with wrinkles. The elemental mapping analysis of the selected region demonstrated the homogeneous dispersion of C and N atoms with negligible amount of oxygen (Fig. 1a), indicating that the oxygen in the air could be hardly incorporated into the g-CN structure. In comparison, a great amount of oxygen in the structures was observed for all doped g-C₃N₄ samples (Fig. 1b–e), which was consistent with elemental analysis (Table S1). These results demonstrated that the interaction of doped metals with urea molecules can readily capture the oxygen of urea into g-C₃N₄ structure. Besides, the metal doping also changed the morphology of g-C₃N₄. The g-CN-Na and g-CN-K exhibited a stacked lamellar agglomerate structure that is hard to be exfoliated probably due to the interactions between g-C₃N₄ layers with the doped Na or K (Fig. 1b–c). For the g-CN-Ca and g-CN-Mg, the warped structure with some irregular pores were observed due to the incomplete polymerization (Fig. 1d–e). In a few cases, this incomplete polymerization led to a broken structure (Fig. S3).

The great change in morphology and elemental composition upon metal doping influenced the BET surface area and pore volume of doped g-C₃N₄. As shown in Fig. 2a, the BET specific surface areas of g-C₃N₄ decrease from 176.7 (g-CN) to 81.2 m² g⁻¹ (g-CN-K) upon doping. This decrease is probably caused by both the agglomerate of doped g-C₃N₄ [6] and the restriction of CO₂ gas release by metals during thermal polymerization. Accordingly, the porous property of g-C₃N₄ also changed upon doping, which was investigated by N₂ adsorption-desorption measurements (Fig. 2b). The BJH pore size distribution curve of g-CN revealed a strong peak at 2.8 nm related to mesopores and a much weaker peak at 55 nm related to macropores. This result indicated that mesopores were predominant in g-CN, which are generated by the gases

release during thermal polymerization. Upon metal doping, the pore volumes of mesopores in all doped g-C₃N₄ were markedly decreased due to the interaction of urea with metals. Additionally, the increased macropore volumes of g-CN-Ca and g-CN-Mg were probably due to incomplete polymerization, whereas negligible macropore volumes of g-CN-Na and g-CN-K were due to their stacked agglomerate structure which is consistent with TEM analysis. These results clearly suggested that the structures of urea-derived g-C₃N₄ were significantly altered by metal doping.

The crystalline structures of the photocatalysts were also investigated by XRD patterns (Fig. 2c). The diffraction peaks of g-CN were consistent well with standard pattern (JCPDS No. 87-1526). The peak of (002) at ca. 26.6° arises from interlayer stacking aromatic systems, and the peak of (100) at ca. 13.1° is related to in-plane repeat of tri-s-triazine units [9,12]. For g-CN-Na and g-CN-K, the (002) peak exhibits red shift with narrowed shape, which has not been reported in the previous studies of alkali metal doped g-C₃N₄ [5,6,10,11]. This feature is quite similar to that of oxidized g-C₃N₄ [13–15], which could be explained by the inserted oxygen atoms and the consequential disturbance of tri-s-triazine units [15]. The insertion of the oxygen can also be supported by the ζ potential measurement (Fig. 2d). Due to the more negative electronic property of O than C and N atoms, ζ potential values of g-CN-Na and g-CN-K remarkably decreased compared to that of the pristine g-C₃N₄. For g-CN-Ca and g-CN-Mg, the diffraction intensities of the (002) peaks were seriously weakened, suggesting an incomplete polymerization and disrupted stacking degree of aromatic layers (Fig. 2c) [16].

The chemical states of the inserted O and the different impacts of metal doping on C and N of as-prepared g-C₃N₄ were further revealed by XPS measurement. In the XPS survey spectra (Fig. 3a), C and N are the main elements in all samples, and the doped metals apparently enhance the amount of O in the doped samples with obvious O 1s peak. The nitrogen element in g-CN (Figs. 3b and S4) are mainly sp²-bonded nitrogen in C=N=C (ca. 398.5 eV, shown in red), the nitrogen in tertiary N-(C)₃ groups (ca. 399.5 eV, shown in blue), and terminal N amines (ca. 400.7 eV, shown in green) [17–19]. As a result of metal doping, the peak area ratios of terminal N to C=N=C dramatically increased from 0.24 to 1.40 and 0.69 in g-CN-Ca and g-CN-Mg, respectively. This result clearly suggested that the interaction of Ca or Mg with urea caused incomplete condensation and increased structural defects [20]. These defects accompanied the formation of two-coordinated carbon C_{2c} which was transformed from the three-coordinated N=C=N (ca. 288.0 eV, Fig. 3c), as evidenced by the emerging C 1s peak at 290.6 eV [21]. Furthermore, an obvious upward shift

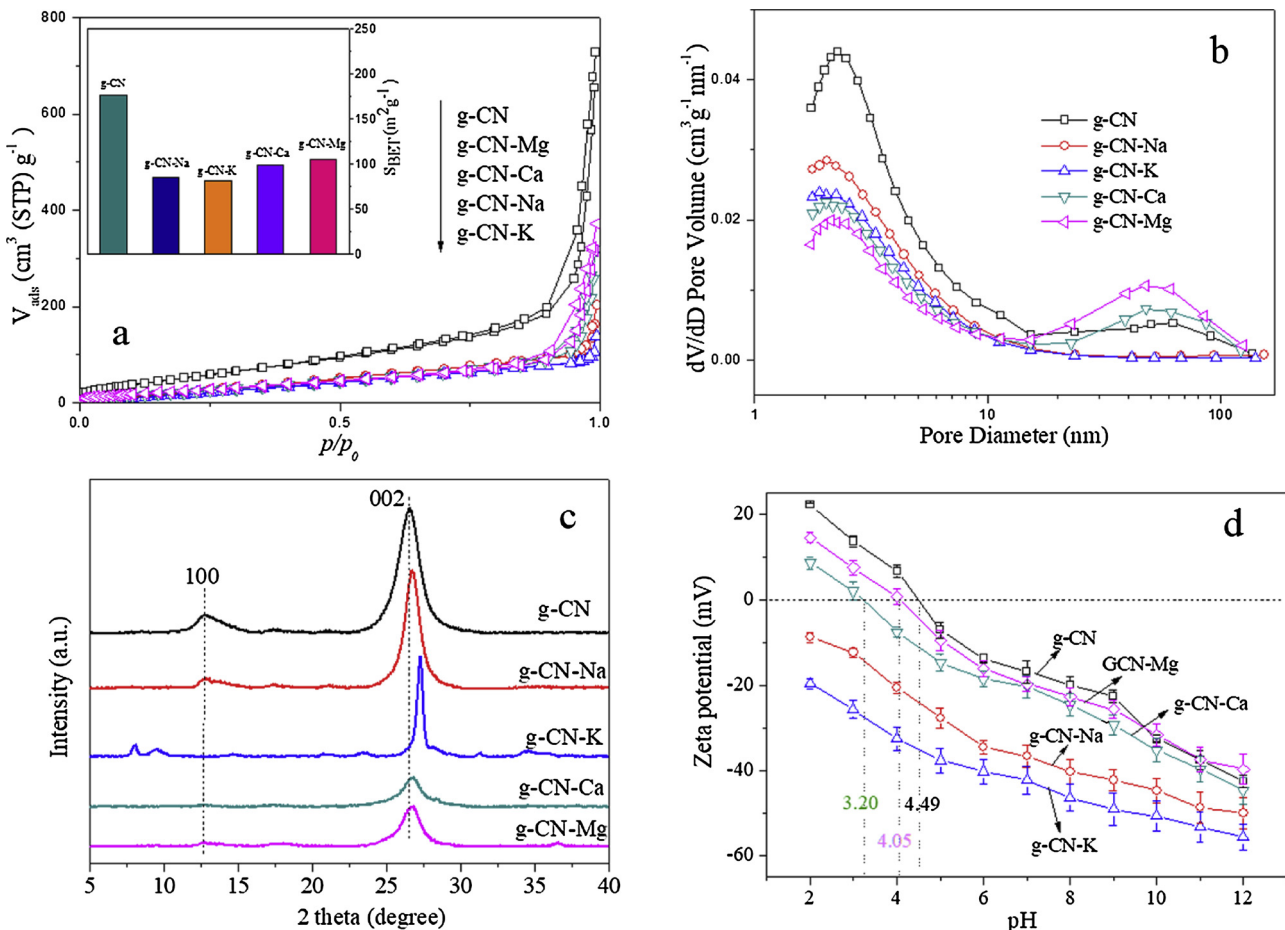


Fig. 2. (a) N₂ adsorption/desorption isotherms, (b) Pore size distribution curves, (c) XRD spectra, and (d) zeta potentials of pristine and doped g-C₃N₄ samples. The inset images of (a) is the BET surface area of these samples. (For interpretation of the references to colour in the text, the reader is referred to the web version of this article.)

was observed in the both N 1s and C 1s spectra for g-CN-Ca and g-CN-Mg (Fig. 3b and c). This is probably due to the partial transferring of the electrons from the lone electron pair of the coordinated nitrogen atoms in the catalyst to the added Ca²⁺ or Mg²⁺, leading to the electron redistribution [7].

By contrast, the Na or K doping presented less impact on the polymerization of g-C₃N₄ (Fig. 3b and c). However, the increased intensity of O 1s signals were observed, compared to that of pristine and Ca or Mg doped g-C₃N₄ (Fig. 3d). Notably, the O 1s peak appeared at 531.0 and 532.8 eV for g-CN-Na and g-CN-K is ascribed to the N—C—O and C—O—C species, respectively [14,22–24], indicating that the O atoms in the g-C₃N₄ lattice directly connected with C atoms rather than N atoms. This result is in agreement with previous DFT study and our ¹³C NMR results (Fig. S5) that O atoms preferentially substitute N atoms and directly bond to C atoms in the doped g-C₃N₄ [25].

The speciation of the doped elements in the catalysts was also determined (Fig. S6). The positions of K 2p_{3/2} (292.8 eV) and K 2p_{1/2} peaks (295.5 eV) for g-CN-K were lower than potassium salt (Fig. S6b) [6], while the g-CN-Na has the same position of the Na 1s (1071.5 eV) to sodium ion (Fig. S6a) [19]. These results indicated that covalent bond between K and g-C₃N₄ was present in g-CN-K, while the doped Na was incorporated in the g-C₃N₄ as a cation. The deconvolution of Ca and Mg 2p line could obtain the similar results that each element contained two species: one was the oxide and the other was ionic species with a higher binding energy due to the ionic character of the bonds (Fig. S6c and d) [26–29].

The chemical bonds of the prepared g-C₃N₄ were further confirmed by the FTIR measurements (Fig. 4). The spectrum of g-CN displays three

characteristic absorption bands, which are located at 810 (the breathing mode of the tris-triazine system), 1200–1800 (C=N and C—N stretching vibration modes), and 3000–3600 cm⁻¹ (O—H of absorbed water and N—H of surface uncondensed amine groups) [30,31]. The doped g-C₃N₄ exhibits the similar characteristic FTIR spectrum to that of g-CN, indicating that their chemical structures are basically consistent. However, the increased intensity of band at 1158 cm⁻¹ and the appearance of the band at 2150 cm⁻¹ in doped g-C₃N₄ was observed, suggesting the addition of O atoms in the frameworks such as C=O and C—O upon elemental doping, especially for g-CN-Na and g-CN-K [32]. Besides, the band at 2180 cm⁻¹, attributed to the stretch vibration of the azide group, were present in the spectra of doped g-C₃N₄, indicating the formation of the band between the structural N with doped metals [19].

3.2. Band structures analysis

The doping process not only significantly changes the bulk structures but also affects the optical and electronic properties of the g-C₃N₄. As shown in Fig. 5a, the UV-vis spectra of g-CN exhibited a visible absorption edge around 440–460 nm. This visible-light response is triggered by the electron transition from the VB populated by N 2p orbitals to the CB formed by hybridized C 2p and N 2p orbitals ($\pi \rightarrow \pi^*$ transitions) [33,34]. Compared to g-CN, absorption edge of doped g-C₃N₄ displayed an obvious red shift, and the band gap of doped g-C₃N₄ was decreased from 2.57 eV to 2.29–2.46 eV, leading to an extended response to visible light (Fig. 5b).

To further confirm the CB and VB potential affected by doping, the

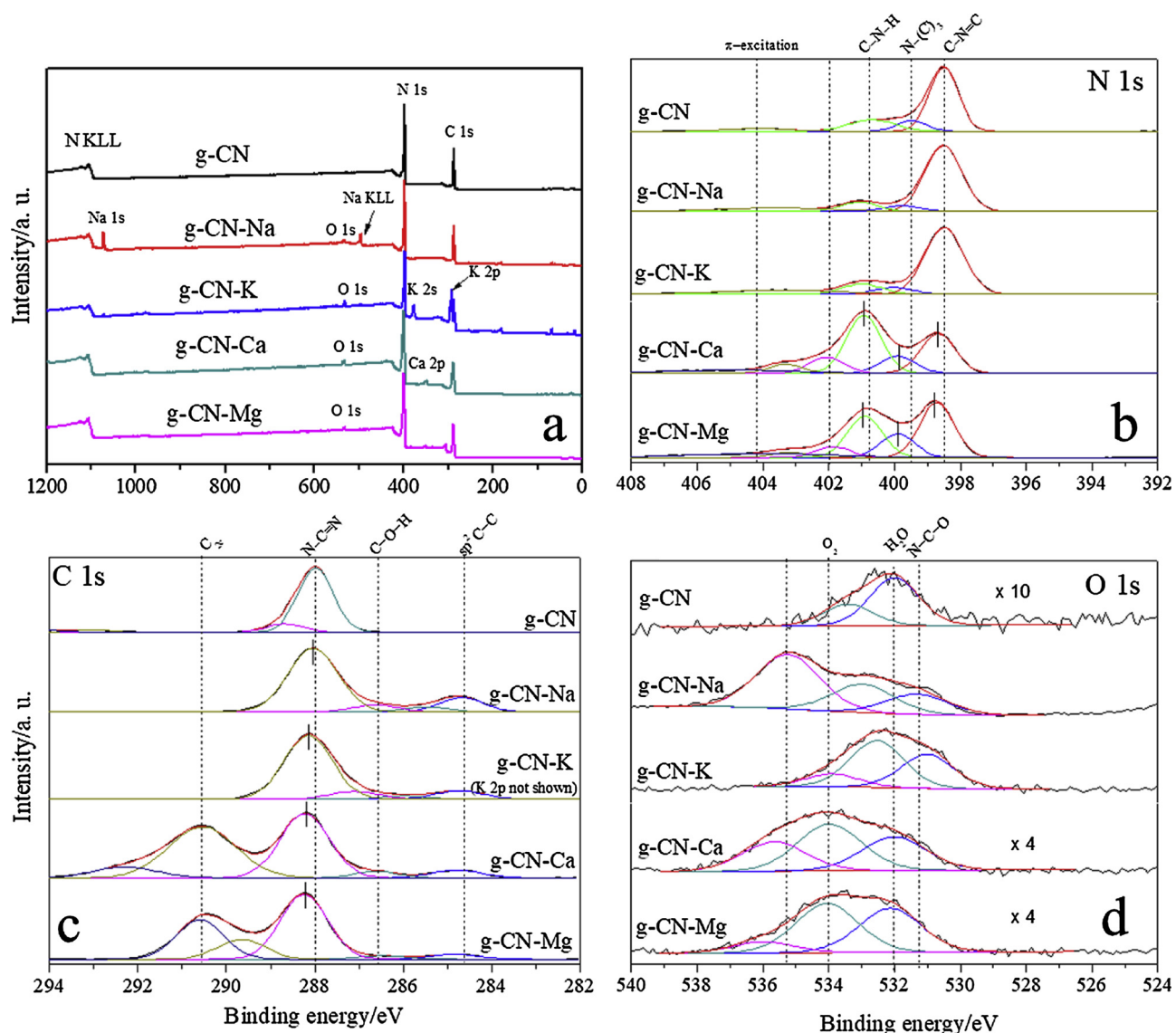


Fig. 3. XPS survey spectrum (a) and the high-resolution XPS spectra expanded for the (b) N 1s, (c) C 1s, (d) O 1s of pristine and doped g-C₃N₄ samples. (For interpretation of the references to colour in the text, the reader is referred to the web version of this article.)

XPS VB analysis was performed. As shown in Fig. 5c, the VB maximum (VBM) edges were located at 1.60, 2.05, 2.12, 1.94, and 1.88 eV for g-CN, g-CN-Na, g-CN-K, g-CN-Ca, g-CN-Mg, respectively. Combined with the results of UV – vis DRS, the CB minimum (CBM) edges were calculated and their band gap structures were shown in Fig. 5d. Notably, due to the synergic effects of doped Na or K and the structural O, the g-CN-Na and g-CN-K possessed more positive VB potential than E⁰ (OH/OH⁻ = 1.99 eV vs NHE), which facilitated the generation of ·OH. In comparison, the sole alkali metal [5,35] or oxygen [36] doped g-C₃N₄ in previous studies did not possess so strong oxidization ability for ·OH generation.

The narrowed bandgap with the obvious downshift of both the VBM and CBM edges of g-CN-Na and g-CN-K could be caused by at least three reasons: (i) the donated electrons by Na and K that combined with N atoms or delocalized within the g-C₃N₄ layers influenced its band gap and band edge position [5]; (ii) the introduction of O in the g-C₃N₄ framework provided extra electrons, resulting in a defect-state lower than CBM after the electronic rearrangement and delocalization [37]; and (iii) the incorporation of O accumulated more electrons around neighboring N atoms in the doped g-C₃N₄, leading to a downshift of VBM edge [23,38]. Therefore, both the introduced Na or K and O in the

g-C₃N₄ framework may affect its VBM and CBM edges.

Similar to Na or K doping, Ca or Mg doping also resulted in the change of the band structure of g-C₃N₄, and g-CN-Ca exhibited an even narrowest bandgap (2.29 eV), which has not been reported previously. Except for the reasons mentioned above, the defects, originated from the incomplete polycondensation, was additional possible reason for the narrowed bandgap of g-CN-Ca and g-CN-Mg. These defects could severe as active sites for surface reaction and introduce additional energy bands between the VB and the CB of g-C₃N₄ [4].

3.3. Optical and photoelectrochemical properties

Apart from the electronic bandgap structure, the separation and transfer of photoexcited charge carriers is also a key factor to determine the photocatalytic efficiency and thus investigated by PL spectra measurements. As shown in Fig. 6a, a broad PL band around 440 nm for g-CN was observed, which was attributed to the band-band recombination of the charge carriers with emission energy equal to its bandgap energy [39]. Upon metal doping, a significant decrease in the PL intensity of doped g-C₃N₄ was observed in the order of K > Na > Mg > Ca. The further quantitative analysis of the charge carrier lifetime

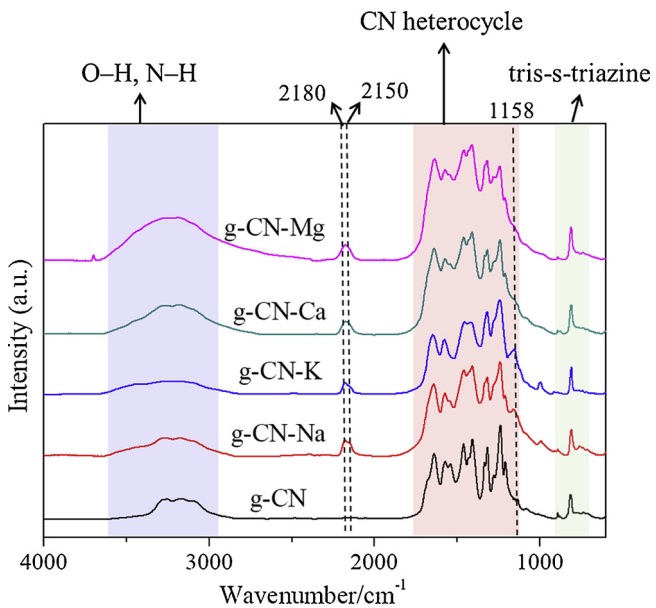


Fig. 4. FTIR spectra of pristine and doped $\text{g-C}_3\text{N}_4$ samples.

by ns time-resolved PL spectra also showed that the PL lifetimes obviously increased upon doping (Fig. 6b, Table 1). The weaker PL emission intensity and prolonged lifetime of charge carriers suggested the inhibited recombination of the photoexcited charge carriers due to the enhanced migration of electron-hole pairs.

The photoelectrochemical measurements provided additional evidences for the efficient separation and transfer of charge carrier on doped $\text{g-C}_3\text{N}_4$. The photoelectric response analysis showed all $\text{g-C}_3\text{N}_4$ samples generated quick and steady photocurrent responses during five times' intermittent on/off irradiation cycles (Fig. 6c). The doped $\text{g-C}_3\text{N}_4$ electrodes exhibited considerably enhanced photocurrent response intensities in comparison with that of undoped $\text{g-C}_3\text{N}_4$, indicating the more electrons could be generated and transferred to the back contact. Further EIS analysis also demonstrated that the diameter of the arc radius on the Nyquist plots of the doped $\text{g-C}_3\text{N}_4$ is smaller than that of the undoped one (Fig. 6d), implying a smaller charge transfer resistance, which led to better electronic conductivity and charge separation efficiency [40].

Notably, the consistent results of PL spectra and photoelectrochemical measurements suggested that the g-CN-Na and g-CN-K exhibited significantly higher improvement in charge carrier separation and transfer than that of g-CN-Ca and g-CN-Mg . Three reasons may account for the promoted efficiency. First, the interactions of doped Na or K with $\text{g-C}_3\text{N}_4$ layers result in an extended π conjugated system that facilitates the migration of delocalized electrons in the conjugated network, leading to an accelerated photocatalytic reactions; second, the lone electron pairs of incorporate O are delocalized in the frameworks, which increased the charge density and mobility [38]; third, the doped Na or K and incorporated O can cause the distortion in the lattice structure of g-CN-Na and g-CN-K , which resulted in an increased surface energy and subsequent a reduced recombination rate for electron-hole pairs [11]. On the other hand, though g-CN-Ca and g-CN-Mg also contain the inserted O atoms in their lattices, the limited capacity to suppress the recombination of the charge carriers was probably due to

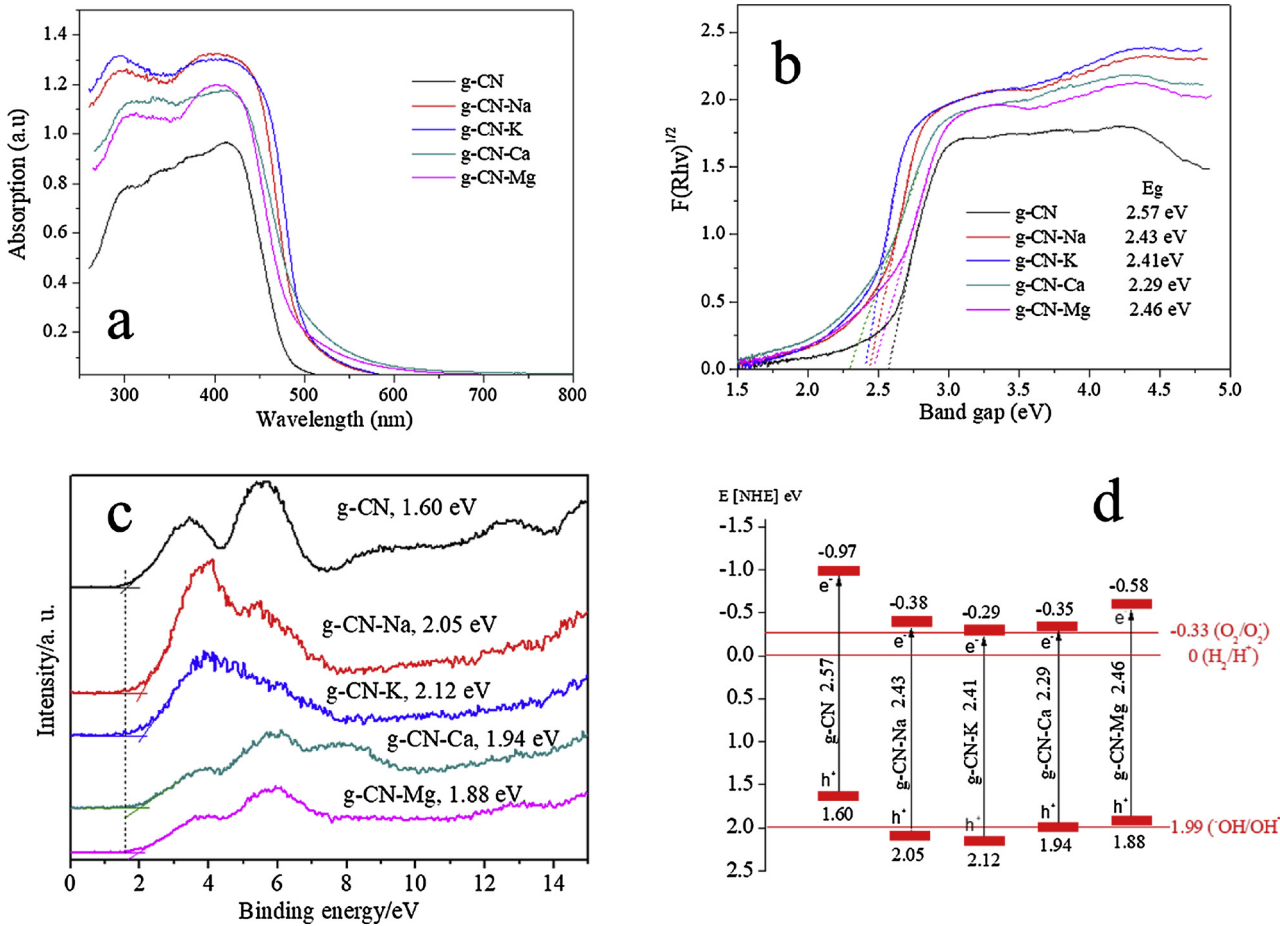


Fig. 5. UV-vis diffuse reflectance spectra (a), the estimated band gap (b), VB XPS (c), and schematic illustration of the band gap structure (d) of pristine and doped $\text{g-C}_3\text{N}_4$ samples.

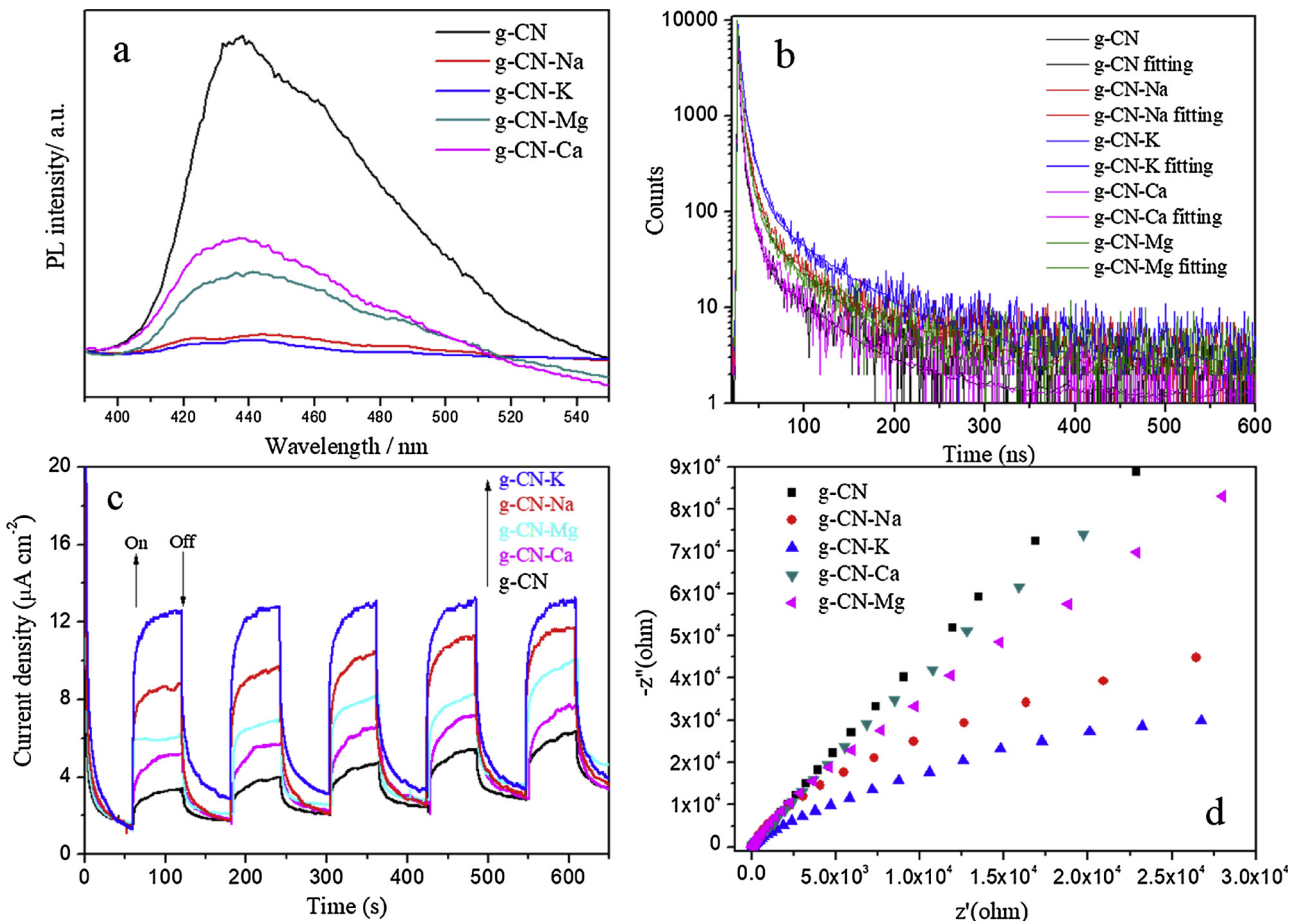


Fig. 6. (a) PL spectra, (b) time-resolved fluorescence spectra, (c) transient photocurrent response, (d) electrochemical impedance spectroscopy of pristine and doped $\text{g-C}_3\text{N}_4$ samples.

Table 1

Fluorescence decay lifetimes and their parameters of photo-excited charge carriers for the $\text{g-C}_3\text{N}_4$ samples.

samples	parameters	lifetimes(ns)	Relative percentage (%)	χ^2
g-CN	τ_1	5.410	86.08	1.168
	τ_2	52.025	13.92	
g-CN-Na	τ_1	6.425	89.92	1.180
	τ_2	75.027	10.08	
g-CN-K	τ_1	6.510	81.05	1.187
	τ_2	64.236	18.95	
g-CN-Ca	τ_1	5.442	85.84	0.957
	τ_2	56.013	14.16	
g-CN-Mg	τ_1	6.118	80.33	0.955
	τ_2	56.529	19.67	

the incomplete condensation and increased defects, which hindered the quick transfer of the delocalized electrons in the structures.

3.4. Enhanced photocatalytic activity

The great change in the morphology, composition, and band structures inevitably impacts the photocatalytic activity of $\text{g-C}_3\text{N}_4$. Fig. 7a displays the pseudo-first-order kinetics of ENR degradation with all prepared $\text{g-C}_3\text{N}_4$ catalysts, according to their calculated removal rate constants (K). In control experiment without $\text{g-C}_3\text{N}_4$ catalyst, negligible ENR was removed within 120 min under visible light irradiation. When $\text{g-C}_3\text{N}_4$ took part in the photoreactions after the adsorption equilibrium, obvious ENR degradation was observed (Fig.S7) and the removal rate constant, $K_{\text{g-CN}}$, is 0.014 min^{-1} . In comparison, this rate constant for

doped $\text{g-C}_3\text{N}_4$ increased by a factor of 3.3 (g-CN-Ca) to 5.4 (g-CN-K), indicating that the photocatalytic activity of $\text{g-C}_3\text{N}_4$ was greatly enhanced by doping (Fig. 7).

Apart from ENR, SMX and TCN, two representative antibiotics with different structure and chemical properties (Fig. S1), were also investigated. Despite different photocatalytic performance for the three antibiotics, the photocatalytic activity of prepared $\text{g-C}_3\text{N}_4$ for each antibiotic was in a similar order of g-CN-K > g-CN-Na > g-CN-Mg > g-CN-Ca > g-CN (Fig. 7).

3.5. Roles of the ROS

It is generally recognized that the photo-induced reactive species may be generated and involved in the photocatalytic reactions, including trapped holes (h^+), $\text{O}_2^{\cdot-}$, and $\cdot\text{OH}$. To verify the contributions of these reactive species, trapping experiments were conducted by adding a scavenger during the photocatalytic process. Triethanolamine (TEOA), *p*-benzoquinone (BZQ), and isopropanol (IPA) were used as scavengers to trap h^+ , $\text{O}_2^{\cdot-}$, and $\cdot\text{OH}$, respectively. As shown in Fig. 8a, the degradation of ENR was significantly inhibited upon BZQ addition but slightly inhibited with the addition of TEOA and IPA for g-CN, g-CN-Ca, and g-CN-Mg, indicating that $\text{O}_2^{\cdot-}$ played dominant role during the degradation process while h^+ as well as $\cdot\text{OH}$ species had minor contributions. For g-CN-Na and g-CN-K, however, both $\text{O}_2^{\cdot-}$ and $\cdot\text{OH}$ species play important roles in ENR degradation, as evidenced by the considerable descend after the addition of BZQ or IPA.

To further provide the direct evidence of the photocatalytically produced $\text{O}_2^{\cdot-}$ and $\cdot\text{OH}$ species by the prepared $\text{g-C}_3\text{N}_4$, ESR spin-trapping experiment were conducted (Fig. 8b and c). DMPO (5,5-

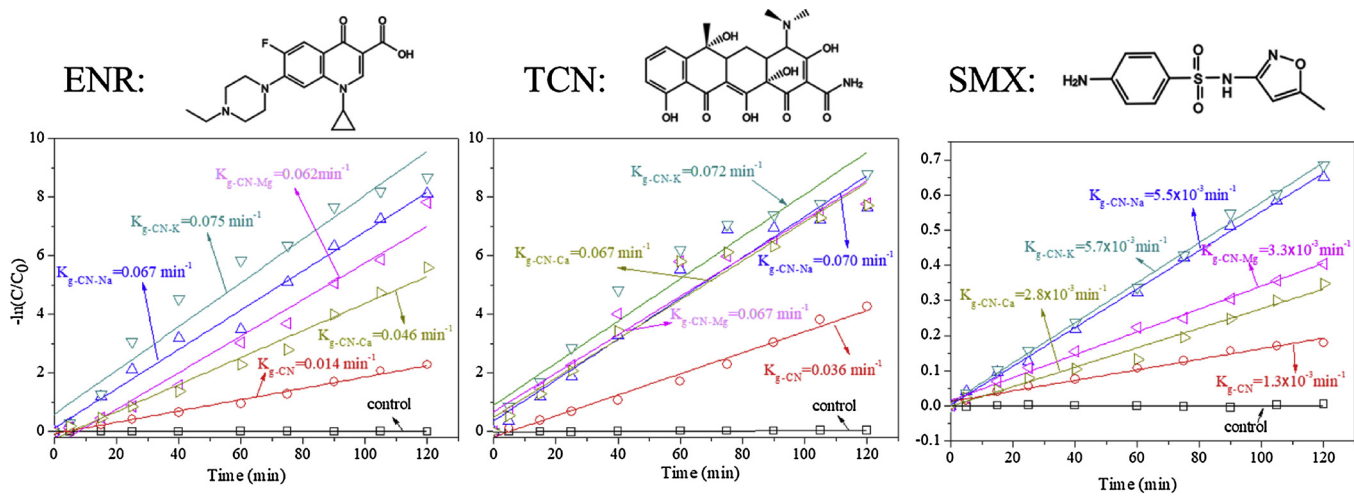


Fig. 7. The photocatalytic activities of as-prepared $\text{g-C}_3\text{N}_4$ samples for (a) ENR, (b) TCN, (c) SMX degradation under visible-light ($\lambda > 420 \text{ nm}$) irradiation.

dimethyl-1-pyrroline N-oxide), was used as trapping reagent for $\cdot\text{OH}$. As displayed in Fig. 8b, no obvious signal was observed in the dark. Under visible light irradiation, the 1:2:2:1 ESR signal with hyperfine splitting parameters of $a^{\text{H}} = a^{\text{N}} = 14.9 \text{ G}$ appeared in the spectra of all $\text{g-C}_3\text{N}_4$ samples, which is characteristic for spin adduct DMPO/ $\cdot\text{OH}$ [41].

It did not mean, however, that all $\text{g-C}_3\text{N}_4$ samples could generate $\cdot\text{OH}$ radical because $\text{O}_2^{\cdot-}$ is unstable in water and may transfer to $\cdot\text{OH}$, leading to the appearance of spin adduct DMPO/ $\cdot\text{OH}$ signals. To deduct the contribution of $\text{O}_2^{\cdot-}$ to the spin adduct signals, superoxide dismutase (SOD) was utilized as $\text{O}_2^{\cdot-}$ scavenger. Fig. 8c displayed that the DMPO/ $\cdot\text{OH}$ signals of g-CN , g-CN-Ca , and g-CN-Mg were appreciably

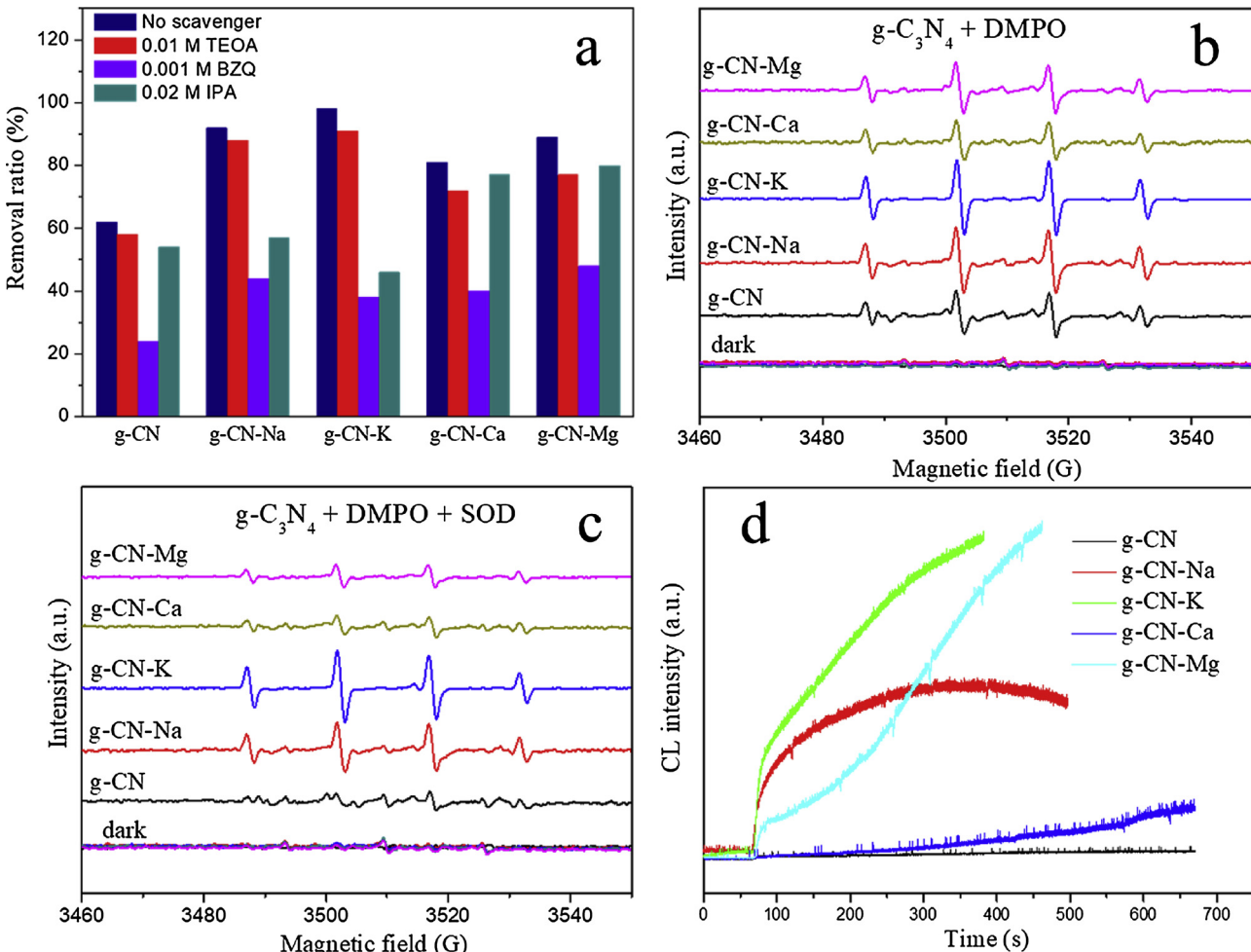


Fig. 8. (a) Trapping experiments of active species for ENR degradation with $\text{g-C}_3\text{N}_4$ photocatalysts. The DMPO spin-trapping ESR spectra in the various $\text{g-C}_3\text{N}_4$ suspensions without (b) or with SOD (c) as $\text{O}_2^{\cdot-}$ scavenger. (d) Online detection of $\text{O}_2^{\cdot-}$ by the various $\text{g-C}_3\text{N}_4$ in 50 μM luminol by using CFCL. All trapping experiments and CFCL detections were under visible-light ($\lambda > 420 \text{ nm}$) irradiation.

suppressed after the addition of SOD. Conversely, strong DMPO·OH signals of g-CN-Na and g-CN-K still remained, verifying the generation of ·OH radical by g-CN-Na and g-CN-K. This result is in agreement with the results of band structure analysis (Fig. 5d).

For specific determination of O_2^- , the continuous flow chemiluminescence (CFCL) method was conducted (detailed in the Supplementary information). As shown Fig. 8d, enhanced CL signals were observed with doped $g\text{-C}_3\text{N}_4$ under visible light irradiation. The generated amount of O_2^- was in the order of g-CN-K > g-CN-Na > g-CN-Ca > g-CN-Mg > g-CN, which was inconsistent with the CB values of these $g\text{-C}_3\text{N}_4$ samples (Fig. 5d). The CFCL results indicated that the generation of O_2^- did not only depend on the band structures but also the separation and transfer efficiency of the photoexcited charge carriers.

3.6. Possible photodegraded intermediates and pathways

To elucidate the photocatalytic characteristics of the prepared $g\text{-C}_3\text{N}_4$, the intermediate products of ENR were identified by HPLC-Q-TOF-MS. During the 120 min reactions under visible light irradiation, a total of twelve intermediate products were identified on the basis of the accurate mass measurement and previous studies [42–44]. The molecular information is listed in the Table S2. Notably, the TOC analysis showed that higher TOC removal rates were observed following protracted irradiation (180 min, Fig. S8), indicating that these ENR intermediates can be further photodegraded and finally mineralized to CO_2 and H_2O .

According to the identified intermediates, the tentative photodegradation pathways of ENR are proposed and presented in Fig. 9. There are two main pathways. Pathway I involves the attack of the piperazine moiety (P1–P12), including the dehydrogenation (P1), oxidation (P9, P10), side-chain dealkylation (P7, P11), cleavage (P2–P5, P8, P12), and final loss of the piperazine ring (P6). Pathway II mainly occurs at the quinolone core (P13–P16), including the decarboxylation (P13), hydrolysis (P14), and cleavage of the quinolone ring (P15).

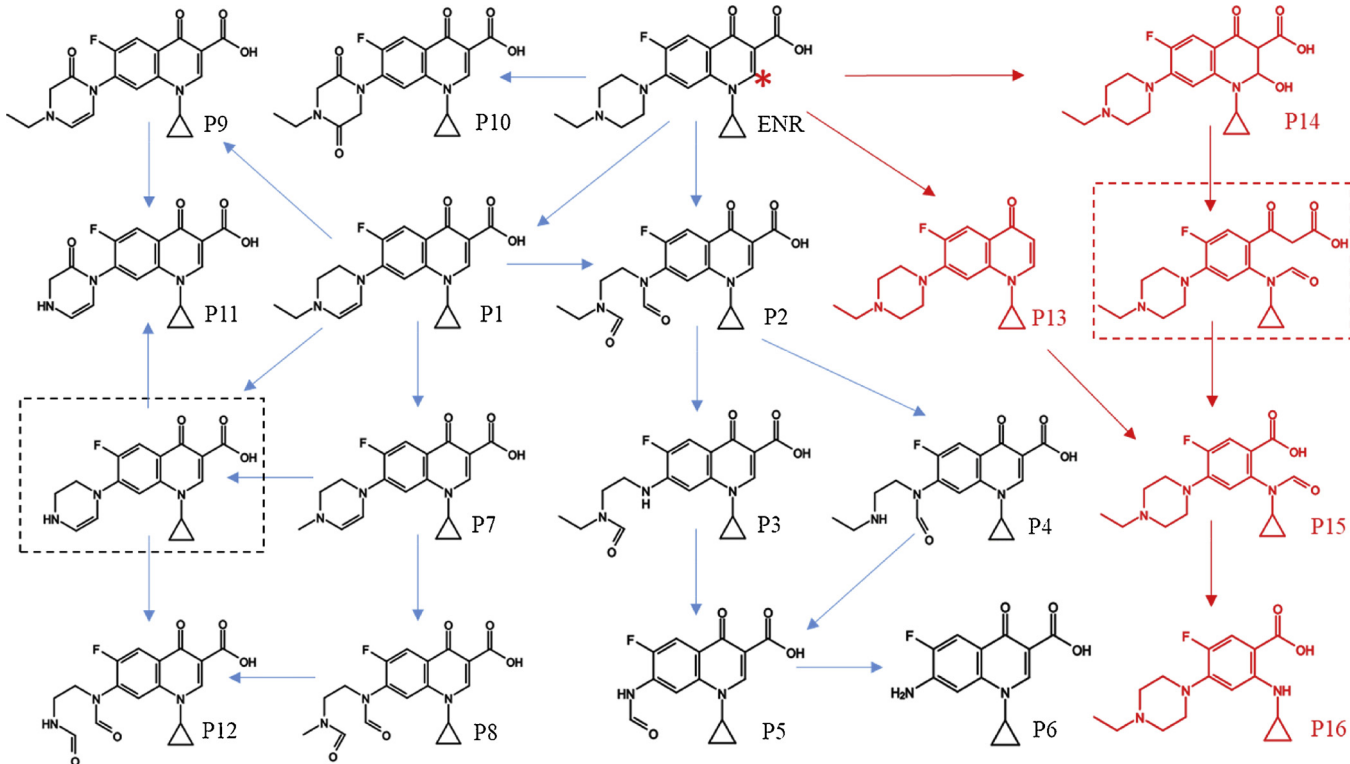


Fig. 9. Proposed photodegradation pathways of ENR in the $g\text{-C}_3\text{N}_4$ suspension under visible light irradiation. (For interpretation of the references to colour in the text, the reader is referred to the web version of this article.)

P16). Interesting, all intermediate products could be detected when g-CN-Na or g-CN-K was present as catalyst, while only the intermediate products of path I were found in the g-CN, g-CN-Ca, and g-CN-Mg photocatalytic reaction systems. It can be attributed to that O_2^- was the main generated ROS by g-CN, g-CN-Ca, and g-CN-Mg and involved in the pathway I reactions, since the O_2^- typically attacked the sites with a more positive point charge [45]. In comparison, ·OH, as well as O_2^- , could be generated by g-CN-Na or g-CN-K and took part in the pathway II reactions. It has been reported the C2 carbon position (labeled by red * in Fig. 9) is most reactive site for ·OH attack in levofloxacin molecule, which is the structural analog to ENR [46].

3.7. Possible mechanism for enhanced photocatalytic activities

Generally, the promoted adsorption on the photocatalyst is an important factor for the enhanced photocatalytic activity since the more adsorbed target molecules lead to the more chance for the photocatalytic reactions. However, our results found that neither the adsorption amount of antibiotics nor the BET specific surface of $g\text{-C}_3\text{N}_4$ were enhanced upon doping treatments (Table S1, Figs. 2a, and S9), which ruled out the possibility that the enhanced photocatalytic activity of $g\text{-C}_3\text{N}_4$ is caused by the enlarged surface areas or improved surfaces with favorable adsorptive properties.

On the other hand, on the basis of the above experimental results, the tentative mechanism responsible for the enhanced photocatalytic degradation of antibiotics by the doped $g\text{-C}_3\text{N}_4$ is elucidated (Fig. 10). Upon visible light irradiation, photoexcited electrons and holes can be generated in the CB and VB of g-CN, respectively (Fig. 10a). Due to the negative CB potential (Fig. 5d), the electrons on the g-CN surfaces can capture the surficial O_2 to form O_2^- , which takes part in the ENR degradation reactions. However, the recombination of electron-hole pairs results in a limited photocatalytic activity. The doping of Na or K in the $g\text{-C}_3\text{N}_4$, and the consequential O introducing into the tri-s-triazine units (Fig. 10b), lead to the extended light absorption range (Fig. 5), improved charge separation efficiency, and prolonged charge lifetimes

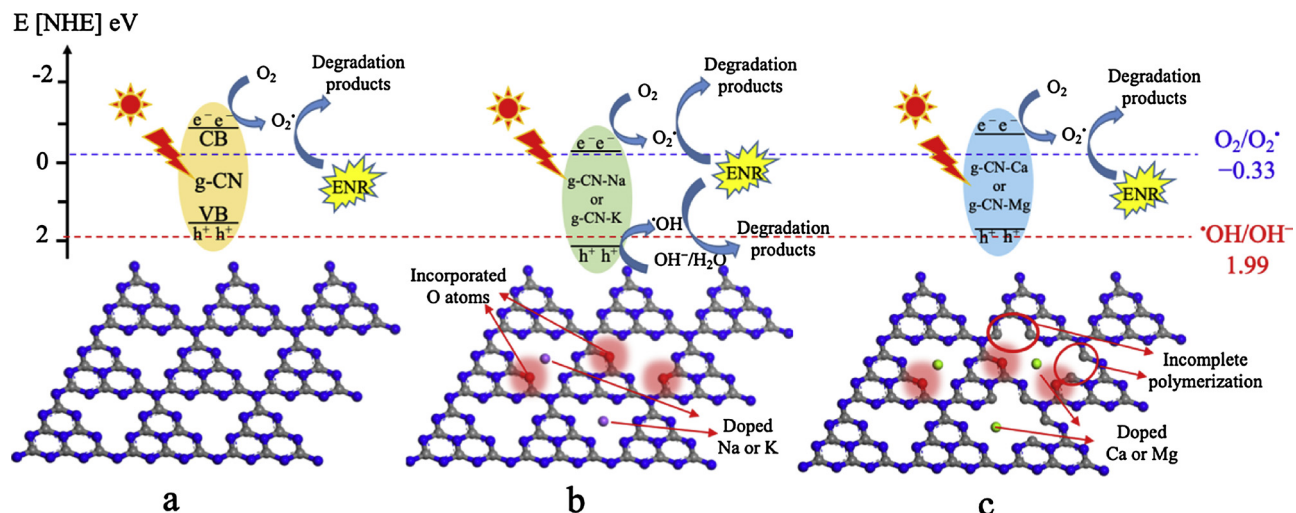


Fig. 10. Schematic diagram of the enhanced photocatalytic degradation of ENR by (a) g-CN, (b) g-CN-Na or g-CN-K, and (c) g-CN-Ca or g-CN-Mg.

(Fig. 6). As a result, more O₂^{•-} can be generated for efficient ENR degradation (Fig. 8). More importantly, the synergistic effects of doped Na or K and the inserted O atoms cause the shift of VB edge (Fig. 5d), which facilitates the photoexcited holes of g-CN-Na or g-CN-K to directly generate ·OH species by the oxidation of OH⁻/H₂O. The attack by ·OH provides additional important photodegradation pathways for ENR (Fig. 9). In comparison, though the doping of Ca or Mg results in narrower band gaps (Fig. 5d), the defects from incomplete polymerization (Fig. 10c), which may act as the recombination centers, greatly impairs the enhancement of photocatalytic activities.

4. Conclusions

The doped urea-derived g-C₃N₄ has been successfully prepared by the simple reaction of metals (Na, K, Ca, Mg) with urea during the polymerization process. The HAADF-TEM images, XPS, and FTIR analysis verify the presence of structural O in the doped g-C₃N₄. These structural O atoms and the doped metals jointly changed the morphology and electronic structures of doped g-C₃N₄, which provided better light-harvesting and reduced charge recombination. As a result, enhanced photocatalytic activity of the doped g-C₃N₄ for antibiotics (ENR, SMX, TCN) degradation was achieved under visible light irradiation. Due to the uneven regulation on the band structures and morphology, however, the photodegradation mechanisms of ENR by various prepared g-C₃N₄ were different. Based on the radical trapping experiments, ESR spin-trapping experiments, and HPLC-Q-TOF-MS analysis, O₂^{•-} was proven to be the predominant active species in the photodegradation systems of g-CN, g-CN-Ca, and g-CN-Mg, whereas both O₂^{•-} and ·OH were generated by g-CN-Na and g-CN-K and played important roles in the photodegradation process. This paper highlights the importance of the interactions between the precursor molecules and the doping components in the doping modification strategy of g-C₃N₄-based photocatalysts. These interactions may result in different physical and electronic structures of doped g-C₃N₄, and thus has significant impact on photocatalytic performance.

Competing financial interest

The authors declare no competing financial interest.

Acknowledgements

We acknowledge the financial support of the National Key Basic Research Program of China (2015CB932003, 2016YFA0203102), the Strategic Priority Research Program of the Chinese Academy of

Sciences (XDB14020302), the National Natural Science Foundation of China (21477144, 21337004, and 21321004).

Appendix A. Supplementary data

Supplementary material related to this article can be found, in the online version, at doi:<https://doi.org/10.1016/j.apcatb.2018.11.069>.

References

- [1] W.D. Oh, V.W.C. Chang, Z.T. Hu, R. Goei, T.T. Lim, Enhancing the catalytic activity of g-C₃N₄ through me doping (Me = Cu, Co and Fe) for selective sulfathiazole degradation via redox-based advanced oxidation process, Chem. Eng. J. 323 (2017) 260–269.
- [2] W.K. Jo, S. Kumar, M.A. Isaacs, A.F. Lee, S. Karthikeyan, Cobalt promoted TiO₂/GO for the photocatalytic degradation of oxytetracycline and Congo Red, Appl. Catal. B: Environ. 201 (2017) 159–168.
- [3] H. Zhang, L.X. Zhao, F.L. Geng, L.H. Guo, B. Wan, Y. Yang, Carbon dots decorated graphitic carbon nitride as an efficient metal-free photocatalyst for phenol degradation, Appl. Catal. B: Environ. 180 (2016) 656–662.
- [4] W.J. Ong, L.L. Tan, Y.H. Ng, S.T. Yong, S.P. Chai, Graphitic carbon nitride (g-C₃N₄)-based photocatalysts for artificial photosynthesis and environmental remediation: are we a step closer to achieving sustainability, Chem. Rev. 116 (2016) 7159–7329.
- [5] T. Xiong, W. Cen, Y. Zhang, F. Dong, Bridging the g-C₃N₄ interlayers for enhanced photocatalysis, ACS Catal. 6 (2016) 2462–2472.
- [6] M. Zhang, X. Bai, D. Liu, J. Wang, Y. Zhu, Enhanced catalytic activity of potassium-doped graphitic carbon nitride induced by lower valence position, Appl. Catal. B: Environ. 164 (2015) 77–81.
- [7] S. Hu, X. Chen, Q. Li, F. Li, Z. Fan, H. Wang, Y. Wang, B. Zheng, G. Wu, Fe³⁺ doping promoted N₂photofixation ability of honeycombed graphitic carbon nitride: the experimental and density functional theory simulation analysis, Appl. Catal. B: Environ. 201 (2017) 58–69.
- [8] Z. Li, C. Kong, G. Lu, Visible photocatalytic water splitting and photocatalytic two-electron oxygen formation over Cu- and Fe-doped g-C₃N₄, J. Phys. Chem. C 120 (2016) 56–63.
- [9] S. Cao, J. Low, J. Yu, M. Jaroniec, Polymeric photocatalysts based on graphitic carbon nitride, Adv. Mater. 27 (2015) 2150–2176.
- [10] J. Zhang, S. Hu, Y. Wang, A convenient method to prepare a novel alkali metal sodium doped carbon nitride photocatalyst with a tunable band structure, RSC Adv. 4 (2014) 62912–62919.
- [11] S. Hu, F. Li, Z. Fan, F. Wang, Y. Zhao, Z. Lv, Band gap-tunable potassium doped graphitic carbon nitride with enhanced mineralization ability, Dalton Trans. 44 (2015) 1084–1092.
- [12] L. Jiang, X. Yuan, Y. Pan, J. Liang, G. Zeng, Z. Wu, H. Wang, Doping of graphitic carbon nitride for photocatalysis: a review, Appl. Catal. B: Environ. 217 (2017) 388–406.
- [13] J. Xu, Z. Wang, Y. Zhu, Enhanced visible-light-driven photocatalytic disinfection performance and organic pollutants degradation activity of porous g-C₃N₄ nanosheets, ACS Appl. Mater. Interface 9 (2017) 27727–27735.
- [14] L. Ming, H. Yue, L. Xu, F. Chen, Hydrothermal synthesis of oxidized g-C₃N₄ and its regulation of photocatalytic activity, J. Mater. Chem. A 2 (2014) 19145–19149.
- [15] L. Yang, J. Huang, L. Shi, L. Cao, Q. Yu, Y. Jie, J. Fei, H. Ouyang, J. Ye, A surface modification resultant thermally oxidized porous g-C₃N₄ with enhanced photocatalytic hydrogen production, Appl. Catal. B: Environ. 204 (2017) 335–345.
- [16] M. Jourshabani, Z. Shariatinia, A. Badiei, Sulfur-doped mesoporous carbon nitride

- decorated with Cu particles for efficient photocatalytic degradation under visible-light irradiation, *J. Phys. Chem. C* 121 (2017) 19239–19253.
- [17] D. Xia, W. Wang, R. Yin, Z. Jiang, T. An Li, G.H. Zhao, P.K. Wong, Enhanced photocatalytic inactivation of *Escherichia coli* by a novel Z-scheme g-C₃N₄/m-Bi₂O₄ hybrid photocatalyst under visible light: the role of reactive oxygen species, *Appl. Catal. B: Environ.* 214 (2017) 23–33.
- [18] L. Shao, D. Jiang, P. Xiao, L. Zhu, S. Meng, M. Chen, Enhancement of g-C₃N₄ nanosheets photocatalysis by synergistic interaction of ZnS microsphere and RGO inducing multistep charge transfer, *Appl. Catal. B: Environ.* 198 (2016) 200–210.
- [19] M. Fronczak, M. Krajewska, K. Demby, M. Bystrzejewski, Extraordinary adsorption of methyl blue onto sodium-doped graphitic carbon nitride, *J. Phys. Chem. C* 121 (2017) 15756–15766.
- [20] X. Long, T. Yan, T. Hu, X. Gong, H. Li, Z. Chu, Enhanced photocatalysis of g-C₃N₄ thermally modified with calcium chloride, *Catal. Lett.* 147 (2017) 1922–1930.
- [21] P. Niu, G. Liu, H.M. Cheng, Nitrogen vacancy-promoted photocatalytic activity of graphitic carbon nitride, *J. Phys. Chem. C* 116 (2012) 11013–11018.
- [22] J.W. Zhang, S. Gong, N. Mahmood, L. Pan, X. Zhang, J.J. Zou, Oxygen-doped nanoporous carbon nitride via water-based homogeneous supramolecular assembly for photocatalytic hydrogen evolution, *Appl. Catal. B: Environ.* 221 (2018) 9–16.
- [23] Z.F. Huang, J. Song, L. Pan, Z. Wang, X. Zhang, J.J. Zou, W. Mi, X. Zhang, L. Wang, Carbon nitride with simultaneous porous network and O-doping for efficient solar-energy-driven hydrogen evolution, *Nano Energy* 12 (2015) 646–656.
- [24] F. Wei, Y. Liu, H. Zhao, X. Ren, J. Liu, T. Hasan, L. Chen, Y. Li, B.L. Su, Oxygen self-doped g-C₃N₄ with tunable electronic band structure for unprecedentedly enhanced photocatalytic performance, *Nanoscale* 10 (2018) 4515–4522.
- [25] B. Zhu, L. Zhang, B. Cheng, J. Yu, First-principle calculation study of tri-s-triazine-based g-C₃N₄: a review, *Appl. Catal. B: Environ.* 224 (2018) 983–999.
- [26] K. Rokosz, T. Hryniwicz, P. Chapon, S. Raaen, H.R.Z. Sandim, XPS and GDOES characterization of porous coating enriched with copper and calcium obtained on tantalum via plasma electrolytic oxidation, *J. Spectrosc.* (2016) 1–7.
- [27] B. Demri, D. Muster, XPS study of some calcium compounds, *J. Mater. Process. Technol.* 55 (1995) 311–314.
- [28] Y. Gofer, R. Turgeman, H. Cohen, D. Aurbach, XPS investigation of surface chemistry of magnesium electrodes in contact with organic solutions of organo-chloroaluminate complex salts, *Langmuir* 19 (2003) 2344–2348.
- [29] S. Ardizzone, C.L. Bianchi, M. Fadoni, B. Vercelli, Magnesium salts and oxide: an XPS overview, *Appl. Surf. Sci.* 119 (1997) 253–259.
- [30] Y. Guo, T. Chen, Q. Liu, Z. Zhang, X. Fang, Insight into the enhanced photocatalytic activity of potassium and iodine codoped graphitic carbon nitride photocatalysts, *J. Phys. Chem. C* 120 (2016) 25328–25337.
- [31] Z.W. Tong, D. Yang, J.F. Shi, Y.H. Nan, Y.Y. Sun, Z.Y. Jiang, Three-dimensional porous aerogel constructed by g-C₃N₄ and graphene oxide nanosheets with excellent visible-light photocatalytic performance, *ACS Appl. Mater. Interface* 7 (2015) 25693–25701.
- [32] X.L. Wang, W.Q. Fang, H.F. Wang, H. Zhang, H. Zhao, Y. Yao, H.G. Yang, Surface hydrogen bonding can enhance photocatalytic H₂ evolution efficiency, *J. Mater. Chem. A* 1 (2013) 14089–14096.
- [33] K. Maeda, X. Wang, Y. Nishihara, D. Lu, M. Antonietti, K. Domen, Photocatalytic activities of graphitic carbon nitride powder for water reduction and oxidation under visible light, *J. Phys. Chem. C* 113 (2009) 4940–4947.
- [34] Y. Chen, B. Wang, S. Lin, Y. Zhang, X. Wang, Activation of n → pi* transitions in two-dimensional conjugated polymers for visible light photocatalysis, *J. Phys. Chem. C* 118 (2014) 29981–29989.
- [35] H. Gao, S. Yan, J. Wang, Y.A. Huang, P. Wang, Z. Li, Z. Zou, Towards efficient solar hydrogen production by intercalated carbon nitride photocatalyst, *Phys. Chem. Chem. Phys.* 15 (2013) 18077–18084.
- [36] Y. Zeng, X. Liu, C. Liu, L. Wang, Y. Xia, S. Zhang, S. Luo, Y. Pei, Scalable one-step production of porous oxygen-doped g-C₃N₄ nanorods with effective electron separation for excellent visible-light photocatalytic activity, *Appl. Catal. B: Environ.* 224 (2018) 1–9.
- [37] S. Guo, Y. Zhu, Y. Yan, Y. Min, J. Fan, Q. Xu, Holey structured graphitic carbon nitride thin sheets with edge oxygen doping via photo-Fenton reaction with enhanced photocatalytic activity, *Appl. Catal. B: Environ.* 185 (2016) 315–321.
- [38] P. Qiu, C. Xu, H. Chen, F. Jiang, X. Wang, R. Lu, X. Zhang, One step synthesis of oxygen doped porous graphitic carbon nitride with remarkable improvement of photo-oxidation activity: role of oxygen on visible light photocatalytic activity, *Appl. Catal. B: Environ.* 206 (2017) 319–327.
- [39] J. Li, B. Shen, Z. Hong, B. Lin, B. Gao, Y. Chen, A facile approach to synthesize novel oxygen-doped g-C₃N₄ with superior visible-light photoreactivity, *Chem. Commun.* 48 (2012) 12017–12019.
- [40] L.K. Putri, B.J. Ng, W.J. Ong, H.W. Lee, W.S. Chang, S.P. Chai, Engineering nanoscale p-n junction via the synergistic dual-doping of p-type boron-doped graphene hybridized with n-type oxygen-doped carbon nitride for enhanced photocatalytic hydrogen evolution, *J. Mater. Chem. A* 6 (2018) 3181–3194.
- [41] W. Yan, J. Zhang, C. Jing, Enrofloxacin transformation on *Shewanella oneidensis* MR-1 reduced goethite during anaerobic-aerobic transition, *Environ. Sci. Technol.* 50 (2016) 11034–11040.
- [42] X.J. Wen, C.G. Niu, L. Zhang, C. Liang, G.M. Zeng, A novel Ag₂O/CeO₂ heterojunction photocatalysts for photocatalytic degradation of enrofloxacin: possible degradation pathways, mineralization activity and an in depth mechanism insight, *Appl. Catal. B: Environ.* 221 (2018) 701–714.
- [43] C. Wang, L. Yin, Z. Xu, J. Niu, L.A. Hou, Electrochemical degradation of enrofloxacin by lead dioxide anode: kinetics, mechanism and toxicity evaluation, *Chem. Eng. J.* 326 (2017) 911–920.
- [44] R.M. Baena-Nogueras, E. Gonzalez-Mazo, P.A. Lara-Martin, Photolysis of antibiotics under simulated sunlight irradiation: identification of photoproducts by high-resolution mass spectrometry, *Environ. Sci. Technol.* 51 (2017) 3148–3156.
- [45] F. Wang, Y. Wang, Y. Feng, Y. Zeng, Z. Xie, Q. Zhang, Y. Su, P. Chen, Y. Liu, K. Yao, W. Lv, G. Liu, Novel ternary photocatalyst of single atom-dispersed silver and carbon quantum dots co-loaded with ultrathin g-C₃N₄ for broad spectrum photocatalytic degradation of naproxen, *Appl. Catal. B: Environ.* 221 (2018) 510–520.
- [46] X. Van Doorslaer, K. Demeestere, P.M. Heynderickx, M. Caussyn, H. Van Langenhove, F. Devlieghere, A. Vermeulen, J. Dewulf, Heterogeneous photocatalysis of moxifloxacin: identification of degradation products and determination of residual antibacterial activity, *Appl. Catal. B: Environ.* 138 (2013) 333–341.